JACS
JOURNAL OF THE AMERICAN CHEMICAL SOCIETY
pubs.acs.org/JACS
Article

Dynamic Metabolons Using Stimuli-Responsive Protein Cages

Wei Kang,[○] Xiao Ma,[○] Huawei Zhang,[○] Juncai Ma, Chunxue Liu, Jiani Li, Hanhan Guo, Daping Wang, Rui Wang, Bo Li, and Chuang Xue*

Cite This: J. Am. Chem. Soc. 2024, 146, 6686−6696
Read Online
ACCESS | Metrics & More | Article Recommendations | Supporting Information

ABSTRACT: Naturally evolved metabolons have the ability to assemble and disassemble in response to environmental stimuli, allowing for the rapid reorganization of chemical reactions in living cells to meet changing cellular needs. However, replicating such capability in synthetic metabolons remains a challenge due to our limited understanding of the mechanisms by which the assembly and disassembly of such naturally occurring multienzyme complexes are controlled. Here, we report the synthesis of chemical- and light-responsive protein cages for assembling synthetic metabolons, enabling the dynamic regulation of enzymatic reactions in living cells. Particularly, a chemically responsive domain was fused to a self-assembled protein cage subunit, generating engineered protein cages capable of displaying proteins containing cognate interaction domains on their surfaces in response to small molecular cues. Chemical-induced colocalization of sequential enzymes on protein cages enhances the specificity of the branched deoxyviolacein biosynthetic reactions by 2.6-fold. Further, by replacing the chemical-inducible domain with a light-inducible dimerization domain, we created an optogenetic protein cage capable of reversibly recruiting and releasing targeted proteins onto and from the exterior of the protein cages in tens of seconds by on−off of blue light. Tethering the optogenetic protein cages to membranes enables the formation of light-switchable, membrane-bound metabolons, which can repeatably recruit−release enzymes, leading to the manipulation of substrate utilization across membranes on demand. Our work demonstrates a powerful and versatile strategy for constructing dynamic metabolons in engineered living cells for efficient and controllable biocatalysis.

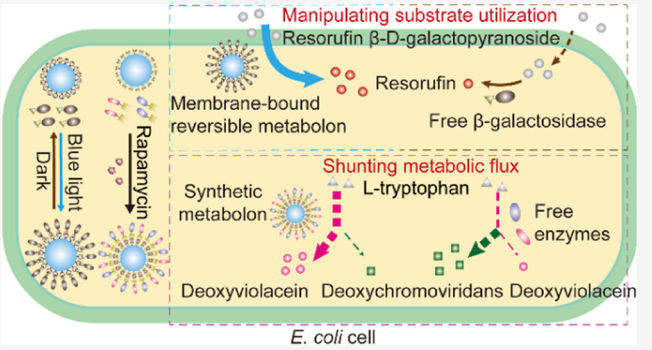

INTRODUCTION

Control over the assembly/disassembly of metabolons is essential to the spatial and temporal regulation of enzymes, enabling the orchestration of chemical reactions within cells.[1,2] In nature, the dynamic assembly of metabolons (e.g., purinosome and Krebs cycle metabolon)[3−5] is elicited by extracellular and intracellular stimuli to redirect metabolism according to changing demands.[6] For example, in sorghum's chemical defense, the formation of a dynamic metabolon, comprising the cytochrome P450 enzymes CYP79A1 and CYP71E1, along with a UDP glucosyltransferase, facilitates the biosynthesis of dhurrin, an anti-insect compound, while the disassembly of this metabolon generates an aldoxime intermediate that serves as an antifungal agent.[7,8] Dynamic metabolons facilitate intermediate transfer between consecutive active sites, inhibit competing reactions, prevent the accumulation of toxic intermediates, and more importantly provide metabolic flexibility and cellular adaptation to cells. However, previous studies have been limited to synthetic metabolons in static form, which used interactive peptides,[9] nucleic acids scaffolds,[10,11] and protein scaffolds[12] to organize targeted enzymes. Although static metabolons have been successful in increasing the yields of desired products, they are limited by their fixed spatial organization of targeted enzymes, compromising their adaptability to dynamically regulate enzymatic reactions.

In contrast to the progress in synthesizing static metabolons, the construction of dynamic metabolons is still limited. Previous research utilized DNA toehold exchange to construct DNA-responsive cellulosome, in which the formation of the metabolon depends on specific DNA triggers.[13] However, the DNA−protein hybrids are not fully genetically encoded, and the delivery may hamper the *in vivo* applications. By repurposing the CRISPR-Cas6 family proteins, a recent study elucidated the construction of stimuli-responsive metabolons in living cells from RNA scaffolds.[14] Unfortunately, due to the limited loading capacity of the RNA scaffolds, only two-enzyme metabolons were generated. In addition, previous work has demonstrated light-responsive metabolons using

Received: November 16, 2023
Revised: February 16, 2024
Accepted: February 16, 2024
Published: March 1, 2024

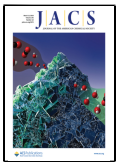

https://doi.org/10.1021/jacs.3c12876
J. Am. Chem. Soc. 2024, 146, 6686−6696

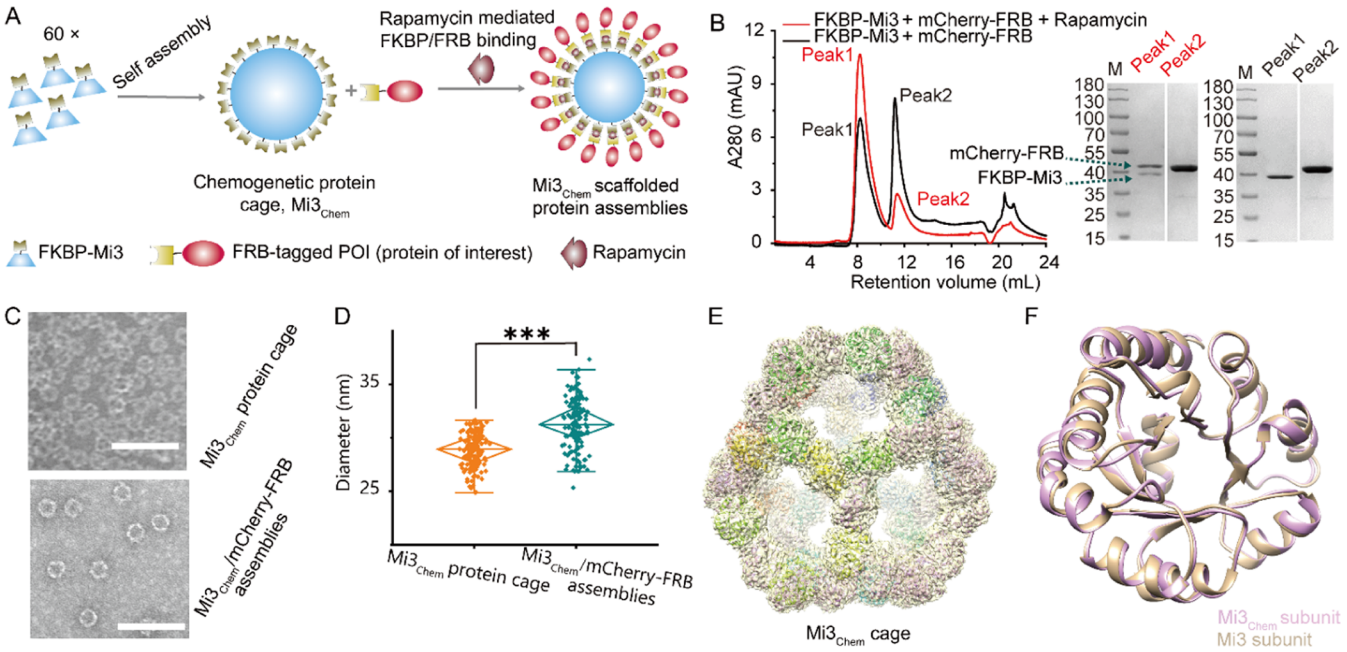

Figure 1. Design and construction of the chemogenetic protein cage $Mi3_{Chem}$. (A) Schematic representation of the chemogenetic protein cage. FKBP-Mi3 fusions readily self-assemble into $Mi3_{Chem}$ protein cages, which can conditionally recruit FRB-tagged cargo proteins in a rapamycin-dependent manner. (B) Size-exclusion chromatography (SEC) profiles of mixtures of FKBP-Mi3 and molar excess of mCherry-FRB in the presence (red line) or absence of rapamycin (black line) and SDS-PAGE analysis of the collected peaks. (C) Negative stained transmission electron microscopy (TEM) of purified $Mi3_{Chem}$ protein cages and $Mi3_{Chem}$ protein cage scaffolded assemblies of mCherry-FRB. Scale bar, 100 nm. (D) Quantification of the particle diameters (n = 150 for each group). Significance was calculated by t test. ***$P < 0.001$. (E) Cryo-EM map and model of the $Mi3_{Chem}$ cage. The map was shown in semitransparency to see the superimposed model. (F) $Mi3_{Chem}$ subunit was superimposed with the previously reported Mi3 subunit (PDB ID: 7b3y).[24] $Mi3_{Chem}$ is shown in magenta. Mi3 is shown in brown.

intrinsically disordered proteins (IDPs) as scaffolds,[15] but the IDPs are often metastable and undergo a phase transition process.[16] To broaden the applications of synthetic metabolons, the ideal scaffolds should have a well-defined structure and high loading capacity, thereby enabling precise control over the assembly/disassembly of the synthetic metabolons and target protein recruitment in response to a specific stimulus.

Protein cages are well-defined, self-assembled nanostructures composed of multiple copies of protein subunits, with multiple attachment sites, excellent biocompatibility, and amenability to genetic modification, which have been engineered as platforms to organize a variety of cargo proteins such as enzymes, fluorophores, and antigens.[17,18] Our recent study has demonstrated the synthesis of static multienzyme metabolons using protein cage Mi3 as scaffolds, resulting in improved catalytic activities.[19] However, a feasible strategy to control the assembly of synthetic metabolons is yet to be achieved.

Here, we successfully synthesized dynamic metabolons by developing stimuli-responsive protein cages, enabling the controllable organization of targeted enzymes on the exteriors of protein cages and leading to the spatial regulation of chemical reactions in prokaryote *Escherichia coli*. We first designed a chemogenetic protein cage ($Mi3_{Chem}$) using a combination of a protein cage subunit and a chemical-induced interaction domain, enabling the recruitment of cargo proteins controlled by rapamycin both *in vitro* and in live cells. Moreover, by replacing the chemical-induced dimerization module with a light-induced dimerization module, we synthesized a light-responsive, optogenetic protein cage, $Mi3_{Opto}$, which can repeatably recruit and release cargo proteins by on−off of the blue light. Importantly, we show that the genetically engineered protein cages can be used to synthesize dynamic metabolons, with applications for directing metabolic flux in a branched reaction and manipulating substrate utilization across membranes, thereby mimicking naturally occurring metabolons to control chemical reactions of cells dynamically. The dynamic metabolons developed in this work expand the toolbox for the spatial and temporal control of protein activities.

RESULTS AND DISCUSSION

Synthesize a Chemogenetic Protein Cage, $Mi3_{Chem}$, for the Chemical-Induced Spatial Organization of Proteins. Living cells can sense the small chemicals in the surrounding environments, achieving dynamic assembly and disassembly of target proteins to coordinate chemical reactions.[20] To mimic the naturally occurring counterparts, we first developed a chemical-responsive protein cage, namely, $Mi3_{Chem}$, to recruit target proteins controlled by small molecules (Figure 1A), based on Mi3, which is a computationally designed, self-assembled protein cage consisting of 60 identical subunits.[21,22] In order to recruit specific target proteins onto protein cages triggered by small molecules, our approach involved the utilization of chemically induced dimerization domains. Specifically, we employed the human FK506-binding protein (FKBP) along with its corresponding FKBP-rapamycin-binding domain (FRB). These domains have gained extensive usage for establishing controlled and inducible interactions between proteins of interest, reliant upon the presence of rapamycin.[23] To this end, FKBP was fused to the surface-exposed N terminus of Mi3 according to the previously reported structure of the Mi3 protein cage (Figure S1), generating a chimeric protein of FKBP-Mi3, whereby the two

https://doi.org/10.1021/jacs.3c12876
J. Am. Chem. Soc. 2024, 146, 6686−6696

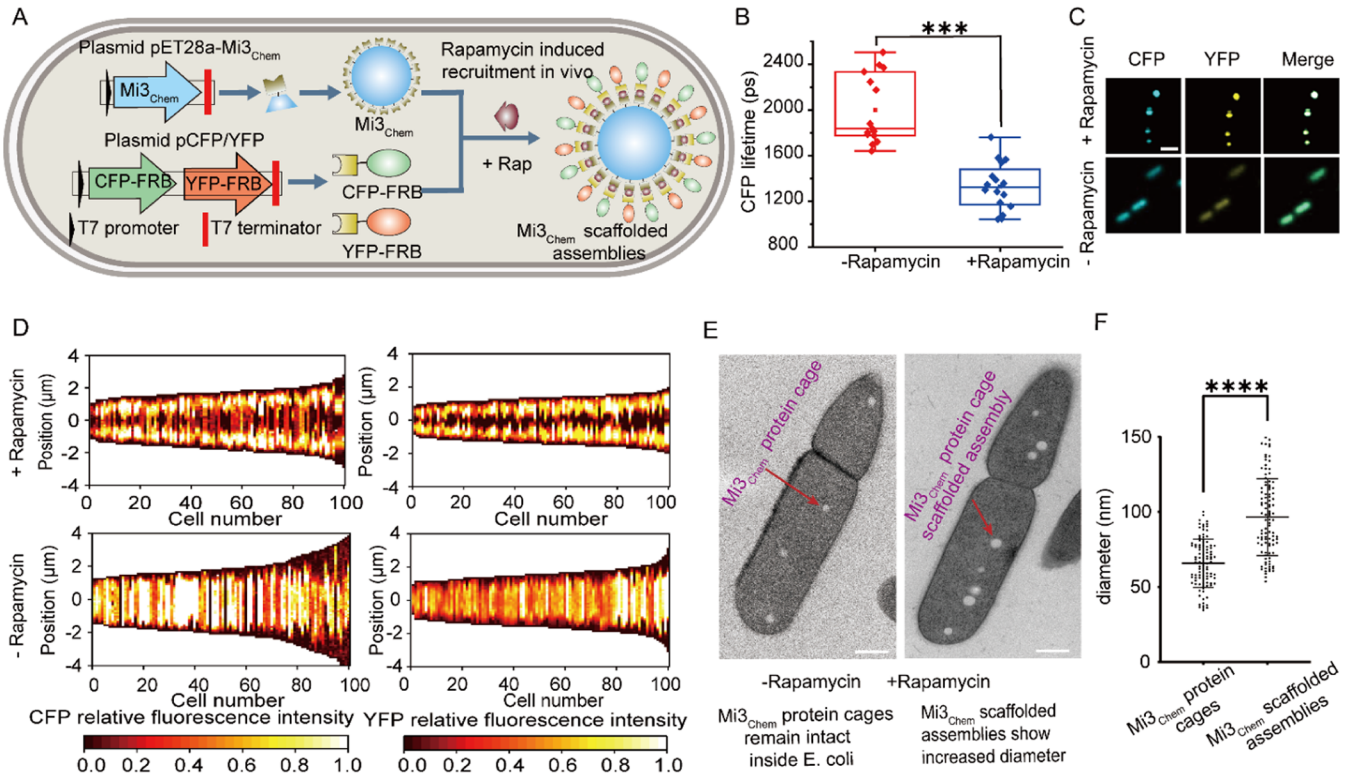

Figure 2. Small molecules induced cargo protein recruitment in living cells. (A) Schematic of chemically inducible recruitment of fluorescent proteins on the chemogenetic $Mi3_{Chem}$ protein cage in living cells. (B) Determination of CFP-FRB lifetime in engineered *E. coli* cells expressing CFP-FRB, FRB-YFP, and FKBP-Mi3 in the presence or absence of rapamycin by fluorescence lifetime imaging microscopy (FLIM). CFP exhibits a shortened lifetime in the presence of rapamycin due to fluorescence resonance energy transfer (FRET) resulting from the rapamycin-induced colocalization of CFP fusions and YFP fusions on protein cages. Significance was calculated by *t* test. ***$P < 0.001$ ($n = 15$ cells for each group). (C) Confocal images of the engineered *E. coli* expressing CFP-FRB, FRB-YFP, and FKBP-Mi3 showing a colocalized fluorescent punctate at the poles of cells in the presence of rapamycin. Cells grown without rapamycin serve as the control showing diffuse fluorescence. Scale bar, 4 μm. (D) Quantification of YFP signals and CFP signals for cells as in (C) showing distinctive fluorescent patterns. Vertical heatmaps representing intensities of fluorescent protein across the long cell axis were generated using microbeJ. Demographs show the fluorescent intensity across a population of cells arranged by cell length. (E) Thin-section TEM images of engineered *E. coli* cells in the presence or absence of rapamycin. Scale bars: 500 nm. (F) Quantification and comparison of diameters of $Mi3_{Chem}$ protein cages and $Mi3_{Chem}$ scaffolded assemblies. *t* test was performed. ****$P < 0.0001$ ($n = 100$ for each group).

modules were connected by a flexible linker (GGS)4 to avoid steric hindrance. As a proof of principle, we employed an FRB-tagged fluorescent protein, mCherry-FRB as a model. FKBP-Mi3 was observed in the soluble fraction, indicating the correct folding of chimera FKBP-Mi3 (Figure S2). Molar excess of mCherry-FRB was mixed with FKBP-Mi3. In the absence of rapamycin, FKBP-Mi3 eluted as a single peak at the void volume by size-exclusion chromatography (SEC), corresponding to supramolecular protein structures (Figure 1B). Morphological analysis of the purified FKBP-Mi3 by transmission electron microscopy (TEM) revealed the presence of well-preserved, spherical nanoparticles measuring approximately 28.9 ± 1.6 nm in diameter (Figure 1C,D), suggesting that the fusion of FKBP to Mi3 does not compromise the inherent capacity of Mi3 to engage in self-directed assembly, maintaining its ability to form protein cages. In contrast, in the presence of rapamycin, SEC and SDS-PAGE showed the co-elution of mCherry-FRB with FKBP-Mi3 (Figure 1B), indicating the chemical-induced recruitment. Further analysis of the collected peaks by Western blot analysis revealed a high loading capacity of the protein cage (Figure S3). TEM analysis of the purified assemblies showed spherical nanoparticles with an increased diameter of 31.3 ± 2.3 nm (Figure 1C,D), indicating the successful, rapamycin-induced recruitment of mCherry-FRB to $Mi3_{Chem}$. In the control experiment, mCherry lacking FRB cannot be recruited to the $Mi3_{Chem}$ even with the addition of rapamycin (Figure S4), indicating that the recruitment was due to the rapamycin-induced interaction between FRB and FKBP rather than rapamycin alone. We also investigated the ability of Mi3 with a C-terminal modification of FKBP (Mi3-FKBP) to serve as a rapamycin-responsive protein cage. However, Mi3-FKBP failed to assemble into a protein cage (Figure S5). Together, these results demonstrate that FKBP-Mi3 chimeras readily self-assemble into a chemically responsive protein cage, $Mi3_{Chem}$, which can recruit target proteins containing the cognate FRB domain in a rapamycin-dependent fashion *in vitro*.

To scrutinize the structural details of $Mi3_{Chem}$, we performed cryo-electron microscopy (cryo-EM) single-particle reconstruction and determined the structure with 3.6 Å resolution (Figures 1E and S6 and Table S1). To the best of our knowledge, this is the first time to report the structure of Mi3 fused with FKBP. To investigate the conformational changes of Mi3 upon fusion with FKBP, a meticulous structural alignment was executed involving the previously reported Mi3 structure (PDB ID: 7b3y)[24] and $Mi3_{Chem}$ cage subunit (Figure 1F). Overall, the Mi3 structure is stable upon being fused with FKBP, with a root mean square deviation (R.M.S.D.) of 0.634

https://doi.org/10.1021/jacs.3c12876
J. Am. Chem. Soc. 2024, 146, 6686−6696

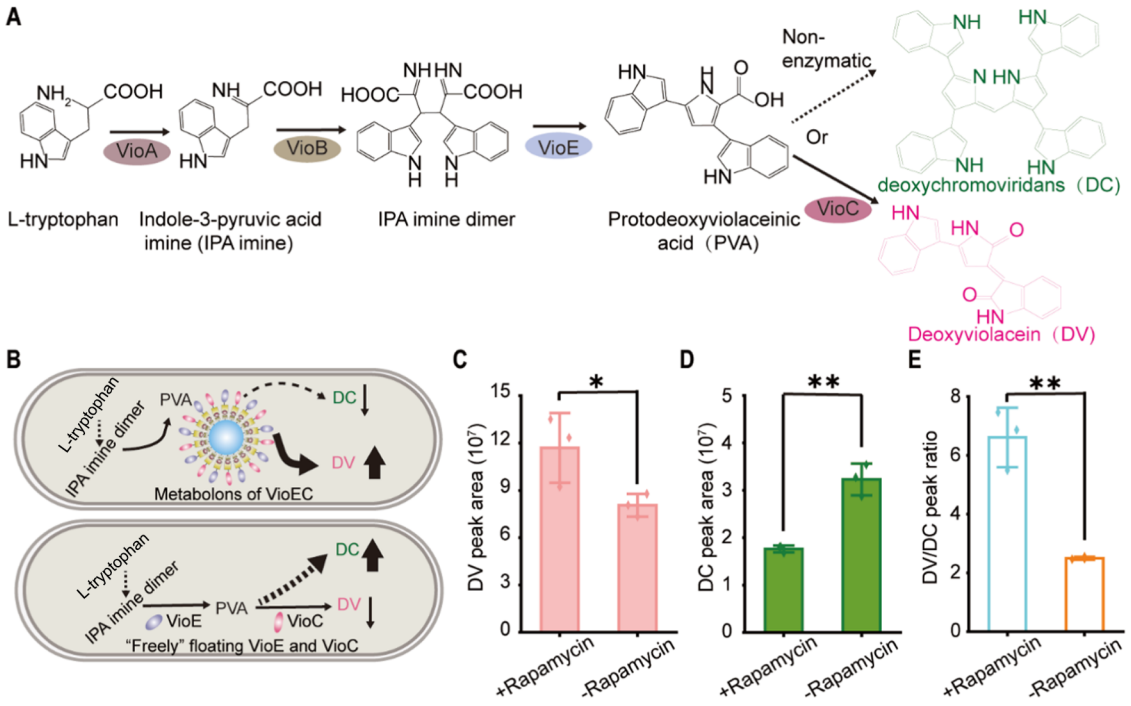

Figure 3. Metabolic shunting at a branched point by synthetic, chemical-responsive metabolons. (A) Schematic diagram of the deoxyviolacein biosynthetic reactions showing a metabolic branch at the intermediate of protodeoxyviolaceinic acid (PVA), which is either enzymatically converted to deoxyviolacein (DV) by VioC, or undergoes a spontaneous, competing reaction to generate deoxychromoviridans (DC). (B) Chemical-induced colocalization of sequential enzymes of VioE-FRB and VioC-FRB by synthetic metabolons is expected to shunt the metabolic flux toward the formation of DV, preventing the formation of DC. (C–E) Rapamycin-induced formation of VioEC metabolons leads to an increase in DV production (C), a decrease in DC production (D), and a higher DV/DC ratio (E). Cells were cultured with or without the addition of 2 μM rapamycin and then harvested 16 h postinduction followed by LC-MS analysis. Significance was calculated by t test. $^{**}P < 0.01$; $^{*}P < 0.05$. Error bars indicate the s.d. of three independent experiments.

Å over 202 Cα atoms. On the other hand, the density of FKBP was not observed in the determined $Mi3_{Chem}$ map, suggesting that the attachment sites (FKBP) are flexible with respect to Mi3, which also indicates that the cargo protein has sufficient space to assemble with $Mi3_{Chem}$ without potential stereo hindrance.

Chemical-Induced Spatial Organization of Proteins in Living Cells. Then, we tested whether $Mi3_{Chem}$ protein cages can recruit cargo proteins in living cells using a FRET (fluorescence resonance energy transfer) pair of CFP and YFP fluorescent proteins as model cargoes (Figure 2A). Plasmid encoding CFP-FRB and FRB-YFP and plasmid encoding FKBP-Mi3 were co-transformed into *E. coli*, and the cells were then examined by fluorescence lifetime imaging microscopy (FLIM). The fluorescence lifetime of CFP-FRB (the donor of the CFP/YFP FRET pair) was significantly shortened in the presence of 2 μM rapamycin compared to that in the absence of rapamycin (1706.4 ps vs 3398.7 ps; Figure 2B) because of the FRET, indicating the rapamycin-induced colocalization of CFP-FRB and FRB-YFP. The distance between the CFP-FRB and FRB-YFP was calculated to be 5.0 nm according to the FRET efficiency (see details in Experimental Section), consistent with the estimated distance (~5 nm) between each attachment site on $Mi3_{Chem}$. In addition, without rapamycin, CFP-FRB and FRB-YFP were evenly distributed over the whole cytoplasm of *E. coli* (Figure 2C,D), consistent with freely floating, cytosolic proteins. In contrast, in the presence of rapamycin, CFP signals and YFP signals were colocalized at the poles of the cells as fluorescent puncta (Figure 2C,D), consistent with the previous observations of concentrated fluorescent signals at the cell poles when fluorescent proteins were assembled to scaffolds.[25,26] We speculate that the formation of fluorescent puncta at the poles of cells may be attributed to the increased size of assemblies of fluorescent proteins relative to freely floating fluorescent proteins, which could lead to the exclusion of the protein assemblies from the center of the cells where the genomic DNA is concentrated. In additional control, engineered cells expressing CFP, YFP, and $Mi3_{Chem}$ constantly generated uniform fluorescence even in the presence of rapamycin (Figure S7). We did not find any cytotoxicity of rapamycin up to 20 μM by monitoring cell growth (Figure S8). We also achieve precise control over the recruitment kinetics by varying the rapamycin concentration (Figure S9). In short, these results indicate that multiple cargo proteins containing the FRB domain can be simultaneously recruited to the $Mi3_{Chem}$ protein cage through chemically induced binding between FKBP and FRB even in complex environments of living cells.

To further confirm the rapamycin-induced cargo recruitment on chemically responsive protein cages in living cells, the engineered cells were characterized by thin-section TEM. In the absence of rapamycin, intact and spherical particles were observed with an average diameter of 65.7 nm (Figure 2E,F), indicating the ability of the FKBP-Mi3 chimera to self-assemble into protein cages even in living cells. In comparison, engineered *E. coli* grown in a medium containing 2 μM rapamycin exhibited spherical particles with an increased average diameter of 96.4 nm (Figure 2E,F), consistent with the successful attachment of fluorescent fusion proteins to the chemogenetic protein cages $Mi3_{Chem}$. The larger diameter of

https://doi.org/10.1021/jacs.3c12876
J. Am. Chem. Soc. 2024, 146, 6686–6696

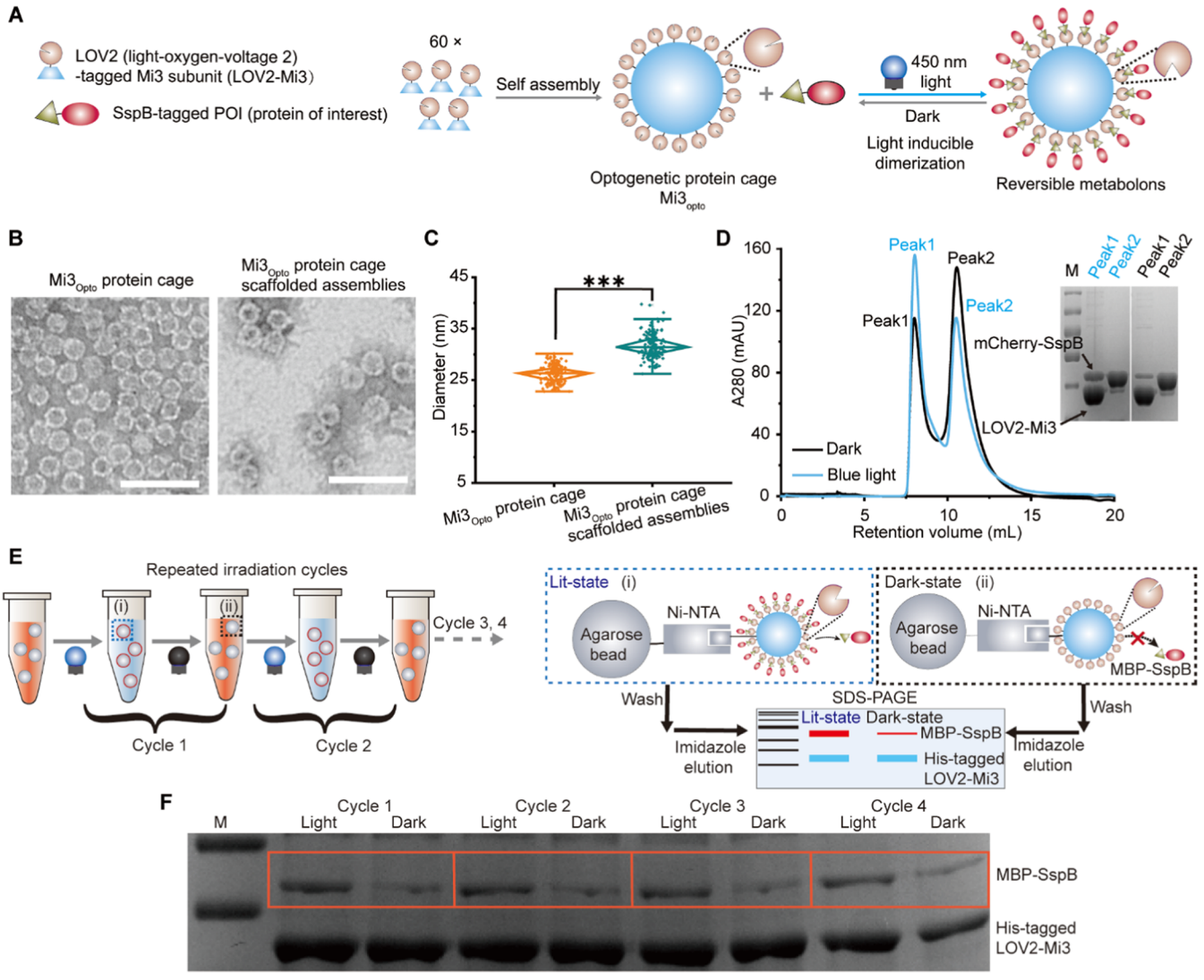

Figure 4. Design and construction of light-responsive protein cage $Mi3_{Opto}$. (A) Schematic of optical control over the reversible recruitment of cargo proteins to optogenetic protein cages $Mi3_{Opto}$ through light-induced interaction between the LOV2 domain and the SspB domain. (B) TEM images of the $Mi3_{Opto}$ protein cage and $Mi3_{Opto}$/mCherry-SspB assemblies. Scale bar: 100 nm. (C) Quantification and comparison of diameters of $Mi3_{Opto}$ protein cages and $Mi3_{Opto}$/mCherry-SspB assemblies (n = 150 for each group). Significance was calculated by t test. ***$P < 0.001$. (D) SEC analysis (left panel) of the $Mi3_{Opto}$ and mCherry-SspB mixture either in the dark (dark line) or under blue-light illumination (blue line). The collected peaks were further analyzed by SDS-PAGE (right panel). More cargo proteins (mCherry-SspB) were bound to the protein cage in the blue light compared to those in the dark. (E) Schematic of *in vitro* pull-down analysis used to investigate the reversibility of the $Mi3_{Opto}$ system. His-tagged $Mi3_{Opto}$ protein cages were immobilized on Ni-NTA agarose beads, followed by the addition of cargo protein of His-tag-free MBP-SspB. Then, the mixture was treated in cycles of blue-light illumination and darkness. Aliquots were removed from the mixture in each step, which were then washed followed by imidazole elution. The eluents were analyzed by SDS-PAGE. Regions outlined in blue and dark dashed lines within the left panel are enlarged on the right panel. (F) SDS-PAGE analysis of the eluents showing reversible recruitment of MBP-SspB to optogenetic $Mi3O_{pto}$ protein cages. The optogenetic protein cage enables at least four cycles of cargo protein recruitment and release.

protein cages determined by thin-section TEM than that of TEM analysis is likely due to the sample preparation process including high-pressure freezing, chemicals fixation, and plastic embedding, which changed the size of the protein. Importantly, we demonstrate that $Mi3_{Chem}$ protein cages organized FRB containing cargo proteins not only *in vitro* but also in living cells.

Control Metabolic Flux in a Branched Pathway by Synthetic, Small Molecule-Responsive Metabolons. Cells precisely regulate reactions through the assembly of metabolons, facilitating spatiotemporal coordination.[27] Inspired by these inherent molecular mechanisms, we harnessed a chemically responsive protein cage as a central platform to orchestrate the sequential arrangement of enzymes, thereby establishing inducible synthetic metabolons capable of governing reaction specificity and yield. To validate this concept, we focused on the deoxyviolacein (DV) biosynthetic reaction, a system characterized by a branching juncture at the intermediate stage of protodeoxyviolaceinic acid (PVA, Figure 3A). PVA is generated by a VioA-, VioB-, and VioE-catalyzed three-step reaction that uses L-tryptophan as substrates. Then, VioC oxidizes PVA to form DV. Alternatively, PVA undergoes a spontaneous, nonenzymatic reaction to give a green byproduct, deoxychromoviridans (DC).

We hypothesized that the PVA flux could be shunted toward enzymatic product DV due to facilitated intermediate transfer

https://doi.org/10.1021/jacs.3c12876
J. Am. Chem. Soc. 2024, 146, 6686−6696

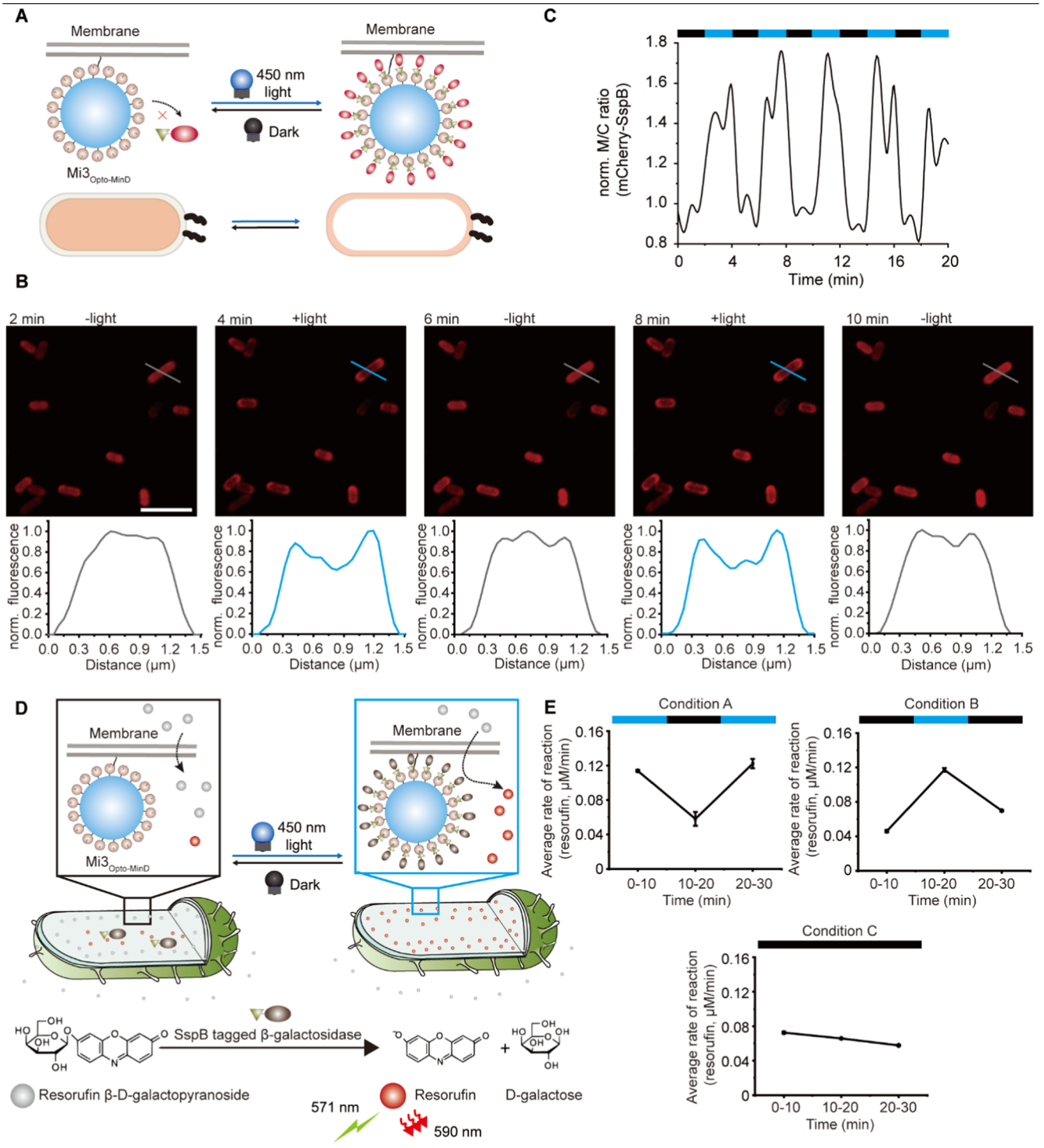

Figure 5. Manipulation of substrate utilization by reversible, membrane-bound metabolons. (A) Schematic of light-dependent recruitment of cargo proteins to membrane-associated protein cages, $Mi3_{Opto\text{-}MinD}$. MinD is used as a membrane-targeting sequence to direct the association of protein cages to the membranes of *E. coli*. The mCherry-SspB model cargo proteins can be targeted to membrane-bound protein cages by light-switchable binding. (B) Time-lapse imaging of cells coexpressing mCherry-SspB and $Mi3_{Opto\text{-}MinD}$ protein cages under cycles of illumination and darkness, showing blue-light-dependent recruitment of mCherry-SspB to membranes (top panels). Bottom panels: Quantification of mCherry-SspB signals along the line cuts. Scale bar, 5 μm. (C) Cycling mCherry-SspB between cytoplasm and membrane over time. Normalized ratios of the membrane to cytoplasm fluorescence intensities (M/C) of mCherry-SspB are plotted against time. The bar on the top indicates when the light is applied (blue) or withdrawn (black). (D) Schematic of membrane-bound reversible metabolons for the regulation of substrate utilization across membranes. Blue-light-dependent recruitment of β-galactosidase to membrane-bound protein cages is expected to control the utilization of the supplemented substrates (resorufin β-D-galactopyranoside), leading to a higher reaction rate when light is applied and vice versa. (E) Average rate of substrate utilization is dependent on light conditions. Cells expressing β-galactosidase and $Mi3_{Opto\text{-}MinD}$ were incubated in indicated light conditions (the bars on top) with the addition of 5 μM resorufin β-D-galactopyranoside. Error bars indicate the s.d. of three independent experiments. Points without error bars have an s.d. too small to show.

https://doi.org/10.1021/jacs.3c12876
J. Am. Chem. Soc. 2024, 146, 6686−6696

by the formation of rapamycin-induced metabolons of VioE and VioC, preventing the diversion of PVA to nonenzymatic product DC (Figure 3B). Therefore, we encoded FRB on the N terminus of the enzymes, yielding fusions of VioE-FRB and VioC-FRB. Plasmid harboring VioA and VioB was also made. Plasmids for DV production and $Mi3_{Chem}$ were co-transformed into *E. coli* cells, generating a DV-producing strain. The products of the engineered pathway were extracted from the cell pellets and then analyzed using LC-MS. With the addition of rapamycin, engineered cells produced 45.1% higher DV, with a concomitant 45.4% decrease in the production of nonenzymatic product DC, relative to that of cells without rapamycin (Figure 3C,D), resulting in a 2.6-fold increase in the DV/DC ratio (Figure 3E). We also confirmed that the protein expression level of VioABCE did not change upon the addition of rapamycin using proteomic analysis (Figure S10). Additionally, we investigated the immobilization effects on enzyme activity using different enzymatic systems *in vitro* (Figures S11 and S12). We observed that assembling an enzyme on protein cages likely did not affect the enzyme activity. Thus, the altered output of the branched DV biosynthetic pathway is likely attributed to the formation of the VioEC metabolon, which effectively enhances metabolic flux toward DV production while impeding the formation of DC. Together, our results underscore the capacity of self-assembled $Mi3_{Chem}$ to modulate the productivity and specificity of the engineered pathway.

Synthesize Optogenetic Protein Cage, $Mi3_{Opto}$ for Light-Controlled Spatial Organization of Proteins. Stimuli-responsive metabolons based on $Mi3_{Chem}$ protein cages are constrained to the conditional formation of metabolons and cannot disassemble due to the irreversible nature of the chemical-induced interactions. In contrast, light-inducible protein−protein interactions offer distinct merits characterized by swiftness, reversibility, and enhanced spatiotemporal accuracy.[28] Thus, we rationally engineer an optogenetic protein cage, $Mi3_{Opto}$, to reversibly assemble and disassemble the synthetic metabolons. We chose to use the iLID system, which consists of a photosensitive domain LOV2 and a short peptide of SspB. LOV2 binds to SspB under blue-light illumination and dissociates in the dark on the time scale of seconds.[29] To this end, the FKBP domain in the FKBP-Mi3 chimera was replaced with the LOV2 domain, yielding LOV2-Mi3. Accordingly, the FRB domain in the target protein was replaced with the SspB domain (Figure 4A). The ability of LOV2-Mi3 to self-assemble into a protein cage was verified by SDS-PAGE, SEC, and TEM (Figures S13 and 4B,C). We also analyzed the detailed structure of $Mi3_{Opto}$ using cryo-EM. The structure of the $Mi3_{Opto}$ protein cage was determined at a resolution of 3.4 Å (Figures S14 and S15 and Table S1). Together, these results demonstrate that the fusion of a photoresponsive protein LOV2 did not perturb the structure of the Mi3 subunit and LOV2-Mi3 can readily self-assemble into protein cages, $Mi3_{Opto}$.

We showed that SspB-tagged proteins could be recruited to the $Mi3_{Opto}$ protein cages in a light-controlled manner by using mCherry-SspB as a model. More mCherry-SspB was coeluted with $Mi3_{Opto}$ protein cage at the void volume under blue-light illumination than that of samples treated in the dark (Figure 4D), indicating the light-dependent recruitment. However, our observations revealed the presence of coeluted mCherry-SspB within the void volume in the dark, suggesting a reduction, albeit not complete elimination, of the interaction between mCherry-SspB and the protein cages (Figure 4D). This unanticipated phenomenon of recruitment is attributed to the inherent "leaky" binding affinity between the LOV2 domain and the SspB domain, a phenomenon frequently encountered in optogenetic tools based on the LOV2 architecture.[30] Nevertheless, this result demonstrates the light-responsive capability of $Mi3_{Opto}$ in recruiting cargo proteins. Subsequent visualization of the purified $Mi3_{Opto}$/mCherry-SspB assemblies by TEM revealed nanoparticles with an increased diameter of 31.7 nm, indicating the formation of light-dependent assemblies *in vitro* (Figure 4B,4C). Thin-section TEM of *E. coli* cells expressing mCherry-SspB and $Mi3_{Opto}$ confirmed the ability of $Mi3_{Opto}$ to self-assemble into intact protein cages, and recruit cargo proteins in a light-dependent manner even in the complex intracellular environment (Figure S16).

We further designed a pull-down analysis to analyze the ability of $Mi3_{Opto}$ protein cages to reversibly recruit cargo proteins during cycles of light illumination and darkness (Figure 4E). To this end, His-tagged $Mi3_{Opto}$ protein cages were immobilized on Ni-NTA agarose beads. The His-tagged MBP-SspB was purified by Ni-NTA affinity purification and then subjected to thrombin cleavage to remove the His tag. The resulting cleaved protein cargoes (His-tag-free MBP-SspB) were then mixed with the beads in either dark or blue light. After that, the beads were washed in the same light conditions, followed by imidazole elution. Finally, the eluents were analyzed by SDS-PAGE. A more intense band corresponding to MBP-SspB was observed for samples that were treated in light, relative to samples that were treated in the dark (Figure 4F), indicating light-induced recruitment of MBP-SspB to protein cages. We found that the light-controlled, reversible recruitment and release could be repeated at least four times. In addition, TEM showed that $Mi3_{Opto}$ protein cages have no distinguishable morphology change after four cycles of illumination, indicating the robustness of the optogenetic protein cages against photoactivation (Figure S17). In short, we reversibly recruit and release cargo proteins via light control *in vitro* and in living cells.

Manipulate Substrate Utilization across Membranes by Reversible Membrane-Bound Metabolons. In biocatalysis, the construction of membrane-bound metabolons is attractive for the efficient utilization of substrates across membranes to increase product yields. Attaching exogenous enzymes in the vicinity of substrate transporters located at membranes allows for the immediate capture and utilization of substrates upon import. Different membrane-bound scaffolds have been developed to construct synthetic metabolons.[26,31] In contrast to the existing approaches, $Mi3_{Opto}$ has the advantage of reversibly recruiting targeted enzymes to construct reversible membrane-bound metabolons, enabling on-demand substrate utilization across membranes.

We first assess the capacity of membrane-bound $Mi3_{Opto}$ to attract the model protein mCherry-SspB (Figure 5A) in living cells by fusing the C-terminal sequence of membrane-targeting protein MinD[32] to LOV2-Mi3 (MinD-LOV2-Mi3), yielding protein cage $Mi3_{Opto\text{-}MinD}$. As expected, mCherry-SspB exhibited diffuse signals in the cytoplasm in dark, whereas they were colocalized with the membrane under blue-light illumination, serving as evidence for the optogenetic protein cage mediated, light-dependent protein translocation from cytoplasm to membranes (Figure 5B). Significantly, with blue light on/off, the distribution of mCherry-SspB switched repeatedly and rapidly on the temporal scale of tens of

https://doi.org/10.1021/jacs.3c12876
J. Am. Chem. Soc. 2024, 146, 6686−6696

seconds between the membrane and cytosol (Figure 5B,C and Movie S1), showing a reversible and repeatable recruitment of targets to the membrane-bound protein cages. Additionally, a control strain expressing $Mi3_{Opto\text{-}MinD}$ protein cage and mCherry without SspB has no response to light, showing constantly diffusible signals in the cytoplasm (Figure S18). We confirmed the ability of MinD-LOV2-Mi3 to self-assemble into intact protein cage $Mi3_{Opto\text{-}MinD}$ by TEM (Figure S19). The findings herein elucidate the capability of reversible recruitment of target proteins to membrane-bound protein cages, contingent upon light stimulation. This, in turn, engenders heightened precision in governing the spatial and temporal dynamics of synthetic metabolons.

We proceeded to inquire into the feasibility of modulating substrate utilization through the establishment of reversible membrane-bound metabolons. As a proof of principle, we chose a β-galactosidase-catalyzed reaction, which converts a nonfluorescent substrate resorufin β-D-galactopyranoside to a red fluorescent product resorufin by hydrolysis (Figure 5D). The fluorogenic reaction allows the monitoring of the reaction by a spectrometric method. To this end, we engineered cells (LacZ-deficient strain) coexpressing β-galactosidase-SspB and $Mi3_{Opto\text{-}MinD}$ and monitored the fluorescent intensity of resorufin. Blue-light illumination increased the fluorescent intensity by nearly 2-fold over the signals of cells in the dark (Figure S20), consistent with the facilitated substrate utilization due to light-dependent recruitment of β-galactosidase to the vicinity of membrane-associated lactose permease where the concentration of substrate is high. The light-induced formation of metabolons of β-galactosidase can disassemble when light is removed and vice versa, thereby enabling the manipulation of the utilization of substrates in a light-dependent manner. To this end, the engineered cells were cultured in different light conditions as shown in Figure 5E. The cells grown in the dark serve as a control (light condition C). In light condition A, we found that cells exhibited a 2-fold increase in the average rate of reaction when blue light was applied (0−10 min), indicating the facilitated substrate utilization by the formation of membrane-bound metabolons. The average rate of reaction decreased to a similar level of the control group when the blue light was removed (10−20 min), indicating the disassembly of the metabolons. Importantly, a nearly 2-fold higher average rate of reaction was again observed when the blue light was applied (20−30 min). A light-dependent average rate of reaction was also detected in light condition B. These studies demonstrate that the assembly and disassembly of metabolons structured by protein cage scaffolds are controlled by light, enabling light-dependent manipulation of the utilization of substrates.

CONCLUSIONS

We offer a new platform for the construction of dynamic metabolons by using stimuli-responsive protein cages. The chimeric proteins consisting of a self-assembled protein cage subunit and an optogenetic/chemogenetic domain self-assembled into monodisperse and intact protein cages with defined structures both *in vitro* and in living cells, as confirmed by SEC, TEM, thin-section TEM, and Cryo-EM. Importantly, the resultant protein cages can conditionally recruit target proteins containing the cognate interaction domain on the exteriors of the protein cages in response to blue light or rapamycin. Given the minimum interference of the sensory domain to the protein cage self-assembly, it is conceivable that the modular approach developed here can be extended to other self-assembled protein materials, thereby endowing them with responsiveness. Furthermore, we demonstrated that the enzyme activities can be spatially controlled by using the stimuli-responsive protein cages, comparable to those of naturally occurring dynamic metabolons. Particularly, rapamycin-induced colocalization of VioE and VioC on stimuli-responsive protein cages enhances the reaction specificity of DV biosynthesis by 2.6-fold. We also demonstrated that the utilization of substrates across membranes can be manipulated by constructing reversible, membrane-bound metabolons. A potential application of the reversible metabolons is to balance the flux of substrates between the exogenous pathways and the endogenous pathways at will, instead of streamlining resources to engineered pathways constantly, which may be deleterious to cell growth. Our study provides the key information for the rational design of dynamic metabolons, which represents a powerful strategy for the spatial regulation of enzyme activities.

EXPERIMENTAL SECTION

Negative Staining TEM. Protein samples were purified and checked using negative staining TEM. Copper grids coated with Formvar carbon films were glow-discharged to increase the hydrophilicity. Ten microliters of the sample with a concentration of about 0.1 mg mL^{-1} was placed on the treated copper grid and incubated for approximately 1 min at room temperature. Excess sample was blotted off with filter paper. The grid was then placed on 10 μL of 1% uranyl acetate stain on the grid for about 20 s, and the excess staining solution was blotted off with filter paper. After the sample was air-dried, the copper grid was placed on a Hitachi HT7700 electron microscope operated at 100 kV under room temperature. Images were taken at a magnification of 40,000.

Cryo-EM Sample Preparation and Data Collection. Peak fractions of FKBP-Mi3 and LOV2-Mi3 from the gel filtration chromatography were concentrated to 1 mg mL^{-1}. Holey carbon 400 mesh 2/2 copper grids were glow-discharged for 60 s with a current of 15 mA using a PELCO easiGlow glow discharge cleaning system (Ted Pella). Four microliters of the sample was applied to the glow-discharged grids and blotted for 3 s with blot force 0 using Vitrobot Mark IV (Thermo Fisher Scientific) operated at 4 °C and 100% humidity. The grids were then plunged into precooled liquid ethane for flash freezing and then transferred to a Titan Krios microscope (Thermo Fisher Scientific) equipped with a Gatan BioQuantum energy filter and K3 Summit detector (Gatan) and operated at 300 kV for sample screening and data collection. Movies were automatically collected in the super-resolution counting mode using EPU software with nominal defocus values ranging from −1.5 to −2.5 μm. The nominal magnifications used for FKBP-Mi3 and LOV2-Mi3 were 105,000× (in different microscopes and cameras), corresponding to calibrated pixel sizes of 0.83 and 0.855 Å, respectively. The total electron dose applied for each movie was 50 e with 32 frames, corresponding to 1.5625 e per frame.

Cryo-EM Data Processing, Model Building, and Refinement. Collected movies were motion-corrected and dose-weighted using MotionCor2.[33] The resulting micrographs were then subjected to input to contrast transfer function (CTF) estimation using CTFFIND4,[34] implied in cryoSPARC.[35] The micrographs were then manually curated to exclude the bad ones. Particles were first autopicked and underwent several rounds of 2D classifications. Good classes were used for training in Topaz[36] to obtain a Topaz model. The model was then used for the second round of particle picking using Topaz. The particles were then extracted and input for 2D classification. Good particles were further used for the initial model building. Heterogeneous refinement was performed for 3D classification, and good classes were further used for nonuniform refinement. Symmetry I was applied during the refinement. Resolutions were estimated using Fourier-shell correlation with a

https://doi.org/10.1021/jacs.3c12876
J. Am. Chem. Soc. 2024, 146, 6686−6696

criterion of 0.143. The previously determined Mi3 structure (PDB ID: 7b3y)[24] was used as the starting model and docked into the cryo-EM maps of FKBP-Mi3 and LOV2-Mi3. The coordinates of docked models were further adjusted in COOT[37] and then subjected to real space refinement in Phenix software.[38] After several rounds of revision, the model was validated using MolProbity.[39] Similar to a previous study,[24] only residues 2−230 of Mi3 were registered and other parts were missing, possibly due to the flexible linker of the fused proteins. Figures were prepared with UCSF Chimera.[40]

Microscopy. Fluorescent imaging of *E. coli* was performed either on an Olympus FV1000 inverted confocal microscope equipped with 405, 488, and 559 nm laser launches, mercury lamp, a ×63 oil immersion objective lens, and a Ma-pmt detector, or on the Zeiss LSM 980 inverted confocal microscope equipped with a laser line module containing 405, 488, and 594 nm lasers, a 63× oil immersion objective lens, and an Airyscan detector, according to experimental requirements. For sample preparation, 1 mL of culture of engineered *E. coli* cells expressing fluorescent proteins was collected by centrifugation. After washing three times with PBS, the cells were resuspended in 200 μL of a minimal medium, and then 2 μL of the sample was added onto a glass slide for imaging. For CFP fluorescence, the samples were excited with a 405 nm laser, and the emission was collected at 460−500 nm. For the YFP signal, fluorescence was detected with excitation at 488 nm and emission capture at 560−610 nm. For the mCherry signal, fluorescence was excited with a 594 laser, and emission was collected from 600 to 670 nm. ImageJ software was used for image analysis and display.

Fluorescence lifetime imaging microscopy (FLIM) analysis was performed on a DCS 120 confocal FLIM system according to our previous study.[19] Briefly, after centrifugation, the collected cells were washed with PBS and then resuspended in a minimal medium for imaging. One microliters of cells was added onto a glass slide for analysis. FRET efficiency E can be calculated by

$$E = 1 - \frac{\tau_{DA}}{\tau_{D}}$$

where τ_{DA} and τ_{D} are the fluorescence lifetimes of the CFP donor in the presence and absence of the acceptor, respectively. The distance between CFP and YFP can be easily calculated from the FRET efficiency with

$$R = R_0 \sqrt[6]{(1 - E)/E}$$

where R_0 is the Förster critical distance and is 5 nm for the CFP/YFP pair.

Mass Spectrometry. For quantification of the products in the deoxyviolacein biosynthetic pathway, 2 mL of the cell culture was collected 7 h after induction by centrifugation at 5000*g* for 10 min. The cell pellets were washed with PBS three times and dried using the SpeedVac concentrator under vacuum. Then, the products of the deoxyviolacein pathway were extracted from the cell pellets with methanol by vortexing the solution for 10 min. After centrifugation at 12,000*g* for 10 min, the clear extraction was subjected to LC-MS analysis using a 6545 LC/Q-TOF mass spectrometer (Agilent) equipped with an AJS ESI source and an Agilent Poroshell 120 SB-C18 column (120 Å, 2.7 μm, 2.1 × 150 mm^2). The samples were eluted at 25 °C with the following gradient program with solvent A: 0.1% (v/v) formic acid in water; solvent B: 100% acetonitrile as the mobile phase at a flow rate of 0.2 mL/min: 5−95% solvent B (0−10 min), 95% solvent B (10−13 min), 95−5% solvent B (13−15 min).

To determine the protein abundance of deoxyviolacein biosynthetic enzymes in engineered cells, a proteomic analysis was performed. Bacterial cultures were collected by centrifugation and then lysed by sonication in PBS. The proteins were reduced and alkylated, digested by trypsin (1:50 weight ratio) at 37°C overnight. After drying, the obtained samples were resuspended in 0.1% FA water and loaded onto the Thermo analytical C18 column (75 μm i.d. × 25 cm) with an Easy-nLC 1200 chromatography pump coupled with Orbitrap Exploris^{TM}480. The spectral data was searched against the defined protein database using PD 2.4 and filtered to 1% FDR (false discovery rate) at the protein level. We used default parameters as follows: a minimum of 1 unique peptide was required for label-free quantitation (LFQ); peptide matching between runs was included and peptides containing oxidation (O), N-terminal acetylation (protein N-term), as dynamic modification and carbamidomethyl (C) as static modification. Only tryptic peptides with two missed cleavage sites were allowed; precursor and fragment mass tolerance were set to 10 ppm and 0.02 Da for MS/MS fragment ions, respectively; and mini and max peptide lengths were 6 and 144.

Thin-Section TEM. For TEM sample preparation, high-pressure freezing, freeze substitution, resin embedding, and ultramicrotomy were performed as described before.[41,42] In brief, the *E. coli* cultures were grown to an optical density (600 nm) of 0.6−0.8 in LB with shaking at 250 r.p.m. Protein expression was induced by IPTG (0.5 mM final) for 16 h at 22 °C with shaking at 250 r.p.m. Cultures were harvested by centrifugation at 6000*g* for 10 min and then rapidly frozen with an EM ICE high-pressure freezer (Leica Microsystems). For Epon resin embedded samples, the samples were freeze-substituted in 2% OsO_4 with acetone at −80 °C for 24 h and then slowly warmed to room temperature over 60 h; excess OsO4 was removed by rinsing with acetone at room temperature. The *E. coli* samples were separated from planchettes and embedded in Embed-812 resin (Electron Microscopy Sciences, Cat. No. 14120) and the resin was polymerized at 65 °C. Ultrathin (90 nm) sections from the samples were collected on copper slot grids coated with Formvar and then examined with a Hitachi 7400 TEM (Hitachi-High Technologies) operated at 80 kV.

■ ASSOCIATED CONTENT

Data Availability Statement

The cryo-EM maps of FKBP-Mi3 and LOV2-Mi3 have been deposited in the Electron Microscopy Data Bank with accession codes EMD-36228 and EMD-36230, respectively. Their corresponding atomic coordinates have been deposited in the Protein Data Bank with accession codes 8JGA and 8JGC, respectively.

Supporting Information

The Supporting Information is available free of charge at https://pubs.acs.org/doi/10.1021/jacs.3c12876.

Movie S1. Light-mediated reversible release and recruitment of mCherry-SspB to membranes by the $Mi3_{Opto\text{-}MinD}$ system. (MP4)

Supporting Information and methods, figures of the structure of Mi3, SDS-PAGE results, Western blot analysis, SEC chromatography profile, Cryo-EM data processing workflows, confocal fluorescence microscopy images, OD_{600} measurements, kinetics of cargo protein recruitment, proteomics analysis, comparison of enzyme activity *in vitro*, Cryo-EM analysis of $Mi3_{Opto}$ protein cage, thin-section TEM analysis, TEM images, tables of Cryo-EM data collection, refinement and validation statistics, nucleotide sequences of the primers, plasmid information, amino acid sequences of the proteins, plasmids construction, strains used in this study, and DNA sequences of the proteins. (PDF)

■ AUTHOR INFORMATION

Corresponding Author

Chuang Xue − *MOE Key Laboratory of Bio-Intelligent Manufacturing, School of Bioengineering, Dalian University of Technology, Dalian 116024, China; Ningbo Institute of Dalian University of Technology, Ningbo 315016, China;* orcid.org/0000-0002-3856-8457; Email: xue.1@dlut.edu.cn

https://doi.org/10.1021/jacs.3c12876
J. Am. Chem. Soc. 2024, 146, 6686−6696

Authors

Wei Kang − *MOE Key Laboratory of Bio-Intelligent Manufacturing, School of Bioengineering, Dalian University of Technology, Dalian 116024, China; Ningbo Institute of Dalian University of Technology, Ningbo 315016, China*

Xiao Ma − *MOE Key Laboratory of Bio-Intelligent Manufacturing, School of Bioengineering, Dalian University of Technology, Dalian 116024, China*

Huawei Zhang − *Shenzhen Institute of Advanced Technology, Chinese Academy of Sciences, Shenzhen 518055, China; Southern University of Science and Technology, Shenzhen 518055, China*

Juncai Ma − *School of Life Sciences, Centre for Cell & Developmental Biology and State Key Laboratory of Agrobiotechnology, The Chinese University of Hong Kong, Hong Kong, China*

Chunxue Liu − *MOE Key Laboratory of Bio-Intelligent Manufacturing, School of Bioengineering, Dalian University of Technology, Dalian 116024, China*

Jiani Li − *MOE Key Laboratory of Bio-Intelligent Manufacturing, School of Bioengineering, Dalian University of Technology, Dalian 116024, China*

Hanhan Guo − *Southern University of Science and Technology, Shenzhen 518055, China*

Daping Wang − *Southern University of Science and Technology, Shenzhen 518055, China*

Rui Wang − *Pingshan Translational Medicine Center, Shenzhen Bay Laboratory, Shenzhen 518118, China;* orcid.org/0000-0003-3830-4133

Bo Li − *Department of Mechanical Engineering, Kennesaw State University, Marietta, Georgia 30060, United States;* orcid.org/0000-0001-9407-9503

Complete contact information is available at: https://pubs.acs.org/10.1021/jacs.3c12876

Author Contributions

○W.K., X.M., and H.Z. contributed equally to this work. All authors have given approval to the final version of the manuscript.

Notes

The authors declare no competing financial interest.

■ ACKNOWLEDGMENTS

Financial support for this work was provided via the National Natural Science Foundation (Nos. 22178046 and U22A20424), the Fundamental Research Fundamental Funds for the Central Universities (Nos. DUT22LAB601 and DUT23YG110), and the Natural Science Foundation of Liaoning Province of China (2022-MS-129).

■ REFERENCES

(1) Greening, C.; Lithgow, T. Formation and function of bacterial organelles. *Nat. Rev. Microbiol.* **2020**, *18*, 677−689.

(2) Agapakis, C. M.; Boyle, P. M.; Silver, P. A. Natural strategies for the spatial optimization of metabolism in synthetic biology. *Nat. Chem. Biol.* **2012**, *8*, 527−535.

(3) Jørgensen, K.; Rasmussen, A. V.; Morant, M.; Nielsen, A. H.; Bjarnholt, N.; Zagrobelny, M.; Bak, S.; Møller, B. L. Metabolon formation and metabolic channeling in the biosynthesis of plant natural products. *Curr. Opin. Plant Biol.* **2005**, *8*, 280−291.

(4) Zhang, Y.; Beard, K. F. M.; Swart, C.; Bergmann, S.; Krahnert, I.; Nikoloski, Z.; Graf, A.; Ratcliffe, R. G.; Sweetlove, L. J.; Fernie, A. R.; Obata, T. Protein-protein interactions and metabolite channelling in the plant tricarboxylic acid cycle. *Nat. Commun.* **2017**, *8*, No. 15212.

(5) French, J. B.; Jones, S. A.; Deng, H.; Pedley, A. M.; Kim, D.; Chan, C. Y.; Hu, H.; Pugh, R. J.; Zhao, H.; Zhang, Y.; Huang, T. J.; Fang, Y.; Zhuang, X.; Benkovic, S. J. Spatial colocalization and functional link of purinosomes with mitochondria. *Science* **2016**, *351*, 733−737.

(6) Sweetlove, L. J.; Fernie, A. R. The role of dynamic enzyme assemblies and substrate channelling in metabolic regulation. *Nat. Commun.* **2018**, *9*, No. 2136.

(7) Møller, B. L. Plant science. Dynamic metabolons. *Science* **2010**, *330*, 1328−1329.

(8) Laursen, T.; Borch, J.; Knudsen, C.; Bavishi, K.; Torta, F.; Martens, H. J.; Silvestro, D.; Hatzakis, N. S.; Wenk, M. R.; Dafforn, T. R.; Olsen, C. E.; Motawia, M. S.; Hamberger, B.; Møller, B. L.; Bassard, J. E. Characterization of a dynamic metabolon producing the defense compound dhurrin in sorghum. *Science* **2016**, *354*, 890−893.

(9) Kang, W.; Ma, T.; Liu, M.; Qu, J.; Liu, Z.; Zhang, H.; Shi, B.; Fu, S.; Ma, J.; Lai, L. T. F.; He, S.; Qu, J.; Wing-Ngor Au, S.; Ho Kang, B.; Yu Lau, W. C.; Deng, Z.; Xia, J.; Liu, T. Modular enzyme assembly for enhanced cascade biocatalysis and metabolic flux. *Nat. Commun.* **2019**, *10*, No. 4248.

(10) Fu, J.; Yang, Y. R.; Johnson-Buck, A.; Liu, M.; Liu, Y.; Walter, N. G.; Woodbury, N. W.; Yan, H. Multi-enzyme complexes on DNA scaffolds capable of substrate channeling with an artificial swinging arm. *Nat. Nanotechnol.* **2014**, *9*, 531−536.

(11) Delebecque, C. J.; Lindner, A. B.; Silver, P. A.; Aldaye, F. A. Organization of intracellular reactions with rationally designed RNA assemblies. *Science* **2011**, *333*, 470−474.

(12) Dueber, J. E.; Wu, G. C.; Malmirchegini, G. R.; Moon, T. S.; Petzold, C. J.; Ullal, A. V.; Prather, K. L.; Keasling, J. D. Synthetic protein scaffolds provide modular control over metabolic flux. *Nat. Biotechnol.* **2009**, *27*, 753−759.

(13) Chen, R. P.; Blackstock, D.; Sun, Q.; Chen, W. Dynamic protein assembly by programmable DNA strand displacement. *Nat. Chem.* **2018**, *10*, 474−481.

(14) Mitkas, A. A.; Valverde, M.; Chen, W. Dynamic modulation of enzyme activity by synthetic CRISPR−Cas6 endonucleases. *Nat. Chem. Biol.* **2022**, *18*, 492−500.

(15) Zhao, E. M.; Suek, N.; Wilson, M. Z.; Dine, E.; Pannucci, N. L.; Gitai, Z.; Avalos, J. L.; Toettcher, J. E. Light-based control of metabolic flux through assembly of synthetic organelles. *Nat. Chem. Biol.* **2019**, *15*, 589−597.

(16) Jawerth, L.; Fischer-Friedrich, E.; Saha, S.; Wang, J.; Franzmann, T.; Zhang, X.; Sachweh, J.; Ruer, M.; Ijavi, M.; Saha, S.; Mahamid, J.; Hyman, A. A.; Jülicher, F. Protein condensates as aging Maxwell fluids. *Science* **2020**, *370*, 1317−1323.

(17) Azuma, Y.; Edwardson, T. G. W.; Hilvert, D. Tailoring lumazine synthase assemblies for bionanotechnology. *Chem. Soc. Rev.* **2018**, *47*, 3543−3557.

(18) Aumiller, W. M.; Uchida, M.; Douglas, T. Protein cage assembly across multiple length scales. *Chem. Soc. Rev.* **2018**, *47*, 3433−3469.

(19) Kang, W.; Ma, X.; Kakarla, D.; Zhang, H.; Fang, Y.; Chen, B.; Zhu, K.; Zheng, D.; Wu, Z.; Li, B.; Xue, C. Organizing Enzymes on Self-Assembled Protein Cages for Cascade Reactions. *Angew. Chem., Int. Ed.* **2022**, *61*, No. e202214001.

(20) Narayanaswamy, R.; Levy, M.; Tsechansky, M.; Stovall, G. M.; O'Connell, J. D.; Mirrielees, J.; Ellington, A. D.; Marcotte, E. M. Widespread reorganization of metabolic enzymes into reversible assemblies upon nutrient starvation. *Proc. Natl. Acad. Sci. U.S.A.* **2009**, *106*, 10147−10152.

(21) Hsia, Y.; Bale, J. B.; Gonen, S.; Shi, D.; Sheffler, W.; Fong, K. K.; Nattermann, U.; Xu, C.; Huang, P. S.; Ravichandran, R.; Yi, S.; Davis, T. N.; Gonen, T.; King, N. P.; Baker, D. Design of a hyperstable 60-subunit protein dodecahedron. *Nature* **2016**, *535*, 136−139.

(22) Bruun, T. U. J.; Andersson, A. C.; Draper, S. J.; Howarth, M. Engineering a Rugged Nanoscaffold to Enhance Plug-and-Display Vaccination. *ACS Nano* **2018**, *12*, 8855−8866.
(23) Stanton, B. Z.; Chory, E. J.; Crabtree, G. R. Chemically induced proximity in biology and medicine. *Science* **2018**, *359*, No. eaao5902.
(24) Tan, T. K.; Rijal, P.; Rahikainen, R.; Keeble, A. H.; Schimanski, L.; Hussain, S.; Harvey, R.; Hayes, J. W. P.; Edwards, J. C.; McLean, R. K.; Martini, V.; Pedrera, M.; Thakur, N.; Conceicao, C.; Dietrich, I.; Shelton, H.; Ludi, A.; Wilsden, G.; Browning, C.; Zagrajek, A. K.; Bialy, D.; Bhat, S.; Stevenson-Leggett, P.; Hollinghurst, P.; Tully, M.; Moffat, K.; Chiu, C.; Waters, R.; Gray, A.; Azhar, M.; Mioulet, V.; Newman, J.; Asfor, A. S.; Burman, A.; Crossley, S.; Hammond, J. A.; Tchilian, E.; Charleston, B.; Bailey, D.; Tuthill, T. J.; Graham, S. P.; Duyvesteyn, H. M. E.; Malinauskas, T.; Huo, J.; Tree, J. A.; Buttigieg, K. R.; Owens, R. J.; Carroll, M. W.; Daniels, R. S.; McCauley, J. W.; Stuart, D. I.; Huang, K. A.; Howarth, M.; Townsend, A. R. A COVID-19 vaccine candidate using SpyCatcher multimerization of the SARS-CoV-2 spike protein receptor-binding domain induces potent neutralising antibody responses. *Nat. Commun.* **2021**, *12*, No. 542.
(25) Giessen, T. W.; Silver, P. A. A catalytic nanoreactor based on in vivo encapsulation of multiple enzymes in an engineered protein nanocompartment. *ChemBioChem* **2016**, *17*, 1931−1935.
(26) Lee, M. J.; Mantell, J.; Hodgson, L.; Alibhai, D.; Fletcher, J. M.; Brown, I. R.; Frank, S.; Xue, W. F.; Verkade, P.; Woolfson, D. N.; Warren, M. J. Engineered synthetic scaffolds for organizing proteins within the bacterial cytoplasm. *Nat. Chem. Biol.* **2018**, *14*, 142−147.
(27) Gou, M.; Ran, X.; Martin, D. W.; Liu, C.-J. The scaffold proteins of lignin biosynthetic cytochrome P450 enzymes. *Nat. Plants* **2018**, *4*, 299−310.
(28) Tischer, D.; Weiner, O. D. Illuminating cell signalling with optogenetic tools. *Nat. Rev. Mol. Cell Biol.* **2014**, *15*, 551−558.
(29) Guntas, G.; Hallett, R. A.; Zimmerman, S. P.; Williams, T.; Yumerefendi, H.; Bear, J. E.; Kuhlman, B. Engineering an improved light-induced dimer (iLID) for controlling the localization and activity of signaling proteins. *Proc. Natl. Acad. Sci. U.S.A.* **2015**, *112*, 112−117.
(30) Gil, A. A.; Carrasco-Lopez, C.; Zhu, L. Y.; Zhao, E. M.; Ravindran, P. T.; Wilson, M. Z.; Goglia, A. G.; Avalos, J. L.; Toettcher, J. E. Optogenetic control of protein binding using light-switchable nanobodies. *Nat. Commun.* **2020**, *11*, No. 4044.
(31) Thomik, T.; Wittig, I.; Choe, J. Y.; Boles, E.; Oreb, M. An artificial transport metabolon facilitates improved substrate utilization in yeast. *Nat. Chem. Biol.* **2017**, *13*, 1158−1163.
(32) Hu, Z.; Lutkenhaus, J. A conserved sequence at the C-terminus of MinD is required for binding to the membrane and targeting MinC to the septum. *Mol. Microbiol.* **2003**, *47*, 345−355.
(33) Zheng, S. Q.; Palovcak, E.; Armache, J. P.; Verba, K. A.; Cheng, Y.; Agard, D. A. MotionCor2: anisotropic correction of beam-induced motion for improved cryo-electron microscopy. *Nat. Methods* **2017**, *14*, 331−332.
(34) Rohou, A.; Grigorieff, N. CTFFIND4: Fast and accurate defocus estimation from electron micrographs. *J. Struct. Biol.* **2015**, *192*, 216−221.
(35) Punjani, A.; Rubinstein, J. L.; Fleet, D. J.; Brubaker, M. A. cryoSPARC: algorithms for rapid unsupervised cryo-EM structure determination. *Nat. Methods* **2017**, *14*, 290−296.
(36) Bepler, T.; Morin, A.; Rapp, M.; Brasch, J.; Shapiro, L.; Noble, A. J.; Berger, B. Positive-unlabeled convolutional neural networks for particle picking in cryo-electron micrographs. *Nat. Methods* **2019**, *16*, 1153−1160.
(37) Emsley, P.; Lohkamp, B.; Scott, W. G.; Cowtan, K. Features and development of Coot. *Acta Crystallogr., Sect. D* **2010**, *66*, 486−501.
(38) Afonine, P. V.; Poon, B. K.; Read, R. J.; Sobolev, O. V.; Terwilliger, T. C.; Urzhumtsev, A.; Adams, P. D. Real-space refinement in PHENIX for cryo-EM and crystallography. *Acta Crystallogr., Sect. D* **2018**, *74*, 531−544.
(39) Williams, C. J.; Headd, J. J.; Moriarty, N. W.; Prisant, M. G.; Videau, L. L.; Deis, L. N.; Verma, V.; Keedy, D. A.; Hintze, B. J.; Chen, V. B.; Jain, S.; Lewis, S. M.; Arendall, W. B., 3rd; Snoeyink, J.; Adams, P. D.; Lovell, S. C.; Richardson, J. S.; Richardson, D. C. MolProbity: More and better reference data for improved all-atom structure validation. *Protein Sci.* **2018**, *27*, 293−315.
(40) Pettersen, E. F.; Goddard, T. D.; Huang, C. C.; Couch, G. S.; Greenblatt, D. M.; Meng, E. C.; Ferrin, T. E. UCSF Chimera–a visualization system for exploratory research and analysis. *J. Comput. Chem.* **2004**, *25*, 1605−1612.
(41) Kang, B.-H. Electron Microscopy and High-Pressure Freezing of Arabidopsis. *Methods Cell Biol.* **2010**, *96*, 259−283.
(42) Ma, J.; Liang, Z.; Zhao, J.; Wang, P.; Ma, W.; Mai, K. K.; Fernandez Andrade, J. A.; Zeng, Y.; Grujic, N.; Jiang, L.; Dagdas, Y.; Kang, B.-H. Friendly mediates membrane depolarization-induced mitophagy in Arabidopsis. *Curr. Biol.* **2021**, *31*, 1931−1944.

https://doi.org/10.1021/jacs.3c12876
J. Am. Chem. Soc. 2024, 146, 6686−6696